

12

VSC-TR-82-13

INVERSION OF SURFACE
WAVES FOR PATH STRUCTURE
AND ATTENUATION

J. Wang
J. L. Stevens
W. L. Rodi
J. B. Minster
B. F. Mason

SYSTEMS, SCIENCE AND SOFTWARE
P. O. Box 1620
La Jolla, California 92038

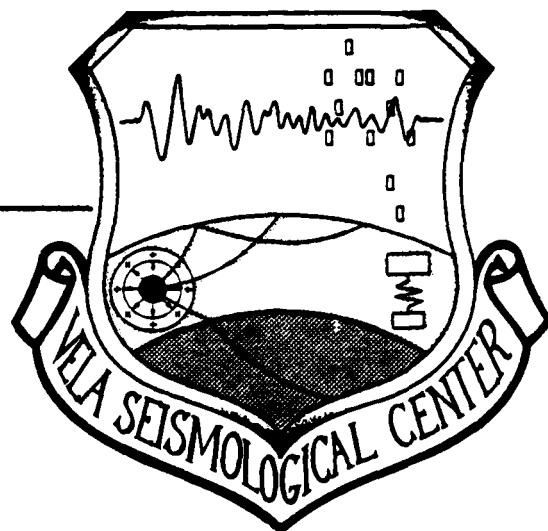
November 1981

TOPICAL REPORT

Approved for Public Release,
Distribution Unlimited.

Monitored by:

VELA Seismological Center
312 Montgomery Street
Alexandria, VA 22314



DTIC
ELECTE
MAR 23 1982
S H D

DTIC FILE COPY

82 03 22 235

ADA112348

Unclassified

SECURITY CLASSIFICATION OF THIS PAGE (When Data Entered)

REPORT DOCUMENTATION PAGE		READ INSTRUCTIONS BEFORE COMPLETING FORM
1. REPORT NUMBER VSC-TR-82-13	2. GOVT ACCESSION NO. AD-A112 348	3. RECIPIENT'S CATALOG NUMBER
4. TITLE (and Subtitle) Inversion of Surface Waves for Path Structure and Attenuation		5. TYPE OF REPORT & PERIOD COVERED Topical Report
		6. PERFORMING ORG. REPORT NUMBER SSS-R-82-5232
7. AUTHOR(s) J. Wang J. L. Stevens W. L. Rodi		8. CONTRACT OR GRANT NUMBER(s) F8606-80-C-0016
9. PERFORMING ORGANIZATION NAME AND ADDRESS Systems, Science and Software P.O. Box 1620 La Jolla, California 92038		10. PROGRAM ELEMENT, PROJECT, TASK AREA & WORK UNIT NUMBERS Program Code No. 1A10 ARPA Order No. 2551
11. CONTROLLING OFFICE NAME AND ADDRESS		12. REPORT DATE November 1981
		13. NUMBER OF PAGES 39
14. MONITORING AGENCY NAME & ADDRESS (if different from Controlling Office) VELA Seismological Center 312 Montgomery Street Alexandria, Virginia 22314		15. SECURITY CLASS. (of this report) Unclassified
		15a. DECLASSIFICATION, DOWNGRADING SCHEDULE
16. DISTRIBUTION STATEMENT (of this Report) Approved for Public Release, Distribution Unlimited.		
17. DISTRIBUTION STATEMENT (of the abstract entered in Block 20, if different from Report)		
18. SUPPLEMENTARY NOTES		
19. KEY WORDS (Continue on reverse side if necessary and identify by block number) Surface waves Path corrections Structure inversion Attenuation		
20. ABSTRACT (Continue on reverse side if necessary and identify by block number) We have developed and tested a set of three computer programs which yield path correction estimates from surface wave observations. The sequence of steps involved in estimating travel path effects on phase and amplitude of a surface wave are: (continued)		

(20. ABSTRACT continued)

1. Retrieval of phase and group velocity dispersion curves from the seismogram by phase matched filtering; extraction of spectral amplitudes by narrow-band filtering; removal of multipath arrivals.
2. Inversion of dispersion curves in terms of an average structure along the path.
3. Calculation of synthetic seismograms from the average structure.
4. Estimation of source moment and attenuation function from synthetic/observed spectral ratios.

Tests on synthetic and real cases show the results of the first three steps to be stable even in the presence of multipathing. In addition, for noise-free data, source moment and attenuation estimates are also reliable. However, the latter quantities are very sensitive to seismic noise and unresolved multipaths so that external constraints on Q models are required for stability.

AFTAC Project Authorization No. VT/0701/B/PMP

ARPA Order No. 2551, Program Code No. 1A10

Effective Date of Contract: 1 April 1981

Contract Expiration Date: 30 September 1982

Amount of Contract: \$1,004,347.00

Contract No. F8606-80-C-0016

Principal Investigators and Phone Nos.

Dr. John M. Savino, (714) 453-0060, Ext. 453

Mr. John R. Murphy, (703) 476-5197

Project Scientist and Phone No.

Mr. Brian W. Barker, (202) 325-7581

This research was supported by the Advanced Research Projects Agency of the Department of Defense and was monitored by AFTAC/VSC, Patrick Air Force Base, Florida, 32925, under Contract No. F08606-80-C-0016.

The views and conclusions contained in this document are those of the authors and should not be interpreted as necessarily representing the official policies, either expressed or implied, of the Advanced Research Projects Agency, the Air Force Technical Applications Center, or the U.S. Government.

S³ Project No. 11143



Accession For	
NTIS GRA&I	<input checked="checked" type="checkbox"/>
DTIC TAB	<input type="checkbox"/>
Unannounced	<input type="checkbox"/>
Justification	
By _____	
Distribution/	
Availability Codes	
Dist	Avail and/or Special
A	

TABLE OF CONTENTS

<u>Section</u>	<u>Page</u>
I. INTRODUCTION AND SUMMARY	1
II. THEORETICAL SURFACE WAVE AMPLITUDES	5
III. PHASE-MATCHED FILTERING	10
IV. TESTS OF PHASE-MATCHED FILTERING USING SYNTHETIC SEISMOGRAMS	14
V. STRUCTURE INVERSION TEST ON SYNTHETIC DATA	19
VI. ATTENUATION, MOMENT ESTIMATES AND INVERSION FOR Q STRUCTURE	28
VII. TEST USING HOGGAR DATA.	31
VIII. COMPUTER CODES	37
IX. OBJECTIVES AND RECOMMENDATIONS	38
X. REFERENCES.	39

LIST OF ILLUSTRATIONS

<u>Figure</u>		<u>Page</u>
1.	Major factors influencing surface wave spectra . . .	7
2.	Flow diagram for determining path corrections. . . .	9
3.	Block diagram, dispersion curve extraction. . . .	13
4.	Eastern United States structure and Rayleigh fundamental-mode dispersion waves.	15
5.	Synthetic seismograms from Eastern United States structure	16
6.	PMF output for S2.. . . .	17
7.	Tradeoff curve	21
8.	Inversion model #1, no crust/mantle discontinuity . .	22
9.	Inversion model #2, discontinuity at 34 km. . . .	24
10.	Inversion model #3, in which the known $\rho(\beta)$ relation is used	25
11.	Dispersion curves from inversion model #2	26
12.	Inverted Q-model and actual Q-model	30
13.	Surface waves from SAPHIRE, February 1965, at Shiraz, Iran (SHI), 4729 km, and Addis Ababa, Ethiopia (AAE), 3948 km	32
14	Inverted velocity-structures from SAPHIRE seismograms: (a) SHI, (b) AAE.. . . .	33
15	Inverted $Q_\beta(z)$ structures from SAPHIRE seismograms: (a) SHI, (b) AAE	35
16	Actual seismograms compared with synthetic seismograms computed from inverted $\beta(z)$ and $Q_\beta(z)$ models: (a) SHI, (b) AAE.	36

LIST OF TABLES

<u>Table</u>		<u>Page</u>
1	ESTIMATED ATTENUATION COEFFICIENTS	29

I. INTRODUCTION AND SUMMARY

We have assembled a set of three computer codes and interfaced them to each other in order to retrieve approximate surface wave path corrections. They are (1) TELVEL, an interactive time series analysis program which extracts dispersion curves and spectral amplitudes from observed wave trains, (2) SWIP, which inverts dispersion curves and attenuation function in terms of an average earth structure along the path, and (3) SURWAV which generates synthetic surface wave trains and spectra for comparison with observations.

The analytical procedure for constructing path corrections comprises four major steps:

1. Group and phase velocity dispersion curves are extracted from each seismogram. A narrow band filtering technique yields an initial estimate of group velocity as a function of frequency. This estimate is then refined through an iterative technique based on phase matched filters (Herrin and Goforth, 1977), which permits retrieval of group and phase velocity dispersion curves after removal of the most severe contamination due to multipathing.
2. The dispersion curves are then inverted for earth structure along the path, as described by Bache, Rodi and Harkrider (1978). Since the data are most sensitive to the shear velocity structure, density and compressional velocity are usually constrained by an empirical relation such as Birch's law. The tradeoff curve between model norm and r.m.s. data misfit can be outlined by performing a single iteration for each value of the tradeoff parameter ϵ and successive iterations are performed for the optimal value of ϵ until convergence is attained.

3. We use this inversion model to compute theoretical unnormalized spectral amplitudes. In the absence of strong lateral variations, these theoretical amplitudes should differ from the observed ones only by a constant proportionality factor times an effective attenuation factor of the form $\exp[-\gamma(\omega)r]$.
4. Comparison of observed and synthetic spectra then permits us to estimate simultaneously the source strength from the spectral ratio at long periods, and the effective attenuation factor as a function of frequency, which can be interpreted in terms of an average Q structure for the path. The overall effectiveness of the procedure can then be assessed by comparing observed and synthetic seismograms.

The results from steps 1 to 3 are relatively robust with respect to minor errors and noise in the data and are thus reliable in most cases. On the other hand, step 4 is much more sensitive to lateral structural variations and unresolved multipathing which are not accounted for in the synthetic calculations, so that Q estimates are much more questionable. The simplest approach for step 4 uses the fact that $\gamma(\omega)$ should vanish in the long period limit. We have verified that this constraint provides acceptable estimates of moment and attenuation function for low-noise records.

We have tested this sequence of programs on a variety of synthetic seismograms, and on two real seismograms.

Synthetic records involving simulated multipathing were constructed using a monopole (explosion) source and an attenuating earth model valid for the eastern U.S. Multipathing was simulated by superposition of synthetic wave trains calculated for several epicentral distances. We applied the procedure outlined above to these synthetic records with the following results.

1. Multipath arrivals were successfully identified and separated by the algorithm whenever the corresponding time delay was about 30 seconds or more. More importantly, even when adequate time resolution could not be achieved, the ensuing bias in dispersion estimates was found to be small. For extreme multipathing (e.g., many narrowly spaced arrivals) the procedure failed to yield a recognizable dispersion curve, but did not result in a stable, but misleading dispersion curve.
2. The inversion of group and phase velocity dispersion recreated the initial "true" structure quite accurately. Numerical experiments show that the selection of a position along the tradeoff curve close to the optimum is fairly important, and that the step involving approximate construction of the tradeoff curve should not be bypassed.
3. Spectral amplitudes of synthetics calculated from the (unattenuating) inversion model match closely the corresponding amplitudes for the "true" structure when attenuation is ignored in the latter. Consequently, comparison of synthetic spectra for the inverted structure with "observed" spectra yielded an estimate of explosion moment $\mu\psi_{\infty}$ accurate to ~ 2 percent, as well as reasonably accurate estimates of $\gamma(\omega)$ at all frequencies (Table 1).

Thus, in the absence of complications other than those included in this test, the method appears to yield acceptable path correction estimates. As a considerably more severe test of the procedure, we also analyzed two seismograms from the Hoggar explosion SAPHIRE, recorded at AAE and SHI.

We were able to retrieve stable dispersion curve estimates in the range 10-50 seconds from both records, and to invert those curves for average path structures. However, comparison of observed and synthetic spectral amplitudes reveals significant contamination from effects not included in the forward modeling. Specifically,

the AAE seismogram seems to be deficient in long period energy, in contrast to the SHI seismogram which has excess long period energy. The SHI record exhibits long period drift which may reflect some instrumental problem. In the case of AAE, we speculate that the proximity of this station to the African Rift Zone may be a source of bias which is not handled well by the procedure.

Although we can formally estimate $\gamma(\omega)$ and $\mu\psi_{\infty}$ from such data, it is clear that these estimates cannot be very reliable, and that a more constrained approach is called for whenever such difficulties arise. Interestingly, such formal estimates lead to a fair match between observed and synthetic wave trains. We are considering two alternatives. The first one is to restrict the range of allowable Q structures based on independent geophysical information, and to achieve a best fit to the observations within this allowable range (e.g., Cheng and Mitchell, 1981). Another alternative consists of a simultaneous interpretation of observations from multiple event-station pairs in terms of a regionalized Q model of the crust and upper mantle. In either case, additional information from independent evidence is called for.

Current efforts are aimed at simplifying input, documenting and streamlining the interfacing of these three codes so as to permit their transfer to the VSC seismic system and begin further testing using high quality digital data.

II. THEORETICAL SURFACE WAVE AMPLITUDES

Harkrider (1964, 1970) formally solved the problem of computing synthetic seismograms from a buried source in a plane-layered earth. Comparison of observed seismograms with synthetic seismograms allows the formulation of the inverse problem of obtaining earth structure, dispersion and source characteristics. The vertical component of the Rayleigh wave displacement (up = positive) from an explosion at depth h is given by the expression (Bache, Rodi and Harkrider, 1978):

$$W(r, \omega) = -4\pi\mu_s \dot{\psi}(\omega) \frac{K_S(h) A_R(\omega)}{c} H_0^{(2)}\left(\frac{\omega r}{c}\right) e^{-\gamma(\omega)r} \left(\frac{r}{R_e \sin \Delta}\right)^{1/2} \quad (1)$$

where

- W = Vertical-component of displacement for fundamental mode Rayleigh wave.
- r = Event-station separation (km).
- ω = Angular frequency.
- μ_s = Source layer shear modulus.
- $\dot{\psi}$ = Reduced velocity potential.
- $K_S(h)$ = Source-depth-dependent modal excitation factor.
- $A_R(\omega)$ = Path structure response.
- c = Phase velocity.
- $H_0^{(2)}$ = Hankel function of the second kind order zero.
- $\gamma(\omega)$ = Anelastic attenuation factor.
- R_e = Earth radius.
- Δ = Event station angular separation.

All factors in this expression are real and positive except for the Hankel function and $\dot{\psi}(\omega)$. All phase information is therefore contained in these two factors. With $\frac{\omega r}{c} \gg 1$, the asymptotic approximation of the Hankel function is

$$-\dot{\psi}(\omega) H_0^{(2)}\left(\frac{\omega r}{c}\right) \approx \dot{\psi}(\omega) \sqrt{\frac{2c}{\pi \omega r}} e^{-i\left(\frac{\omega r}{c} + \frac{3\pi}{4}\right)} \quad (2)$$

Furthermore, for small values of ω , the phase of $\dot{\psi}(\omega)$ is small; so almost all of the phase information is contained in the exponential function. Given the distance r , the phase velocity $c(\omega)$ and group velocity $u(\omega)$ are recovered from the phase spectrum using the method of phase-matched filters (Section III).

The phase and group velocity dispersion curves are inverted for earth structure following the method of Bache, Rodi and Harkrider (1978). This inversion depends only on the phase function of the seismogram (Figure 1). The earth structure may then be used to compute the unknown quantities $A_R(\omega)$ and $K_S(h)$ in Equation (1). Of course, the source depth h is usually not known, but since $K_S(h)$ is a slowly varying function for small h , an approximate depth estimate is usually adequate.

In the long period limit $\psi(\omega) \approx \psi_\infty$, a positive constant. Evaluation of Equation (1) at an observation point with $\gamma(\omega) = 0$ and $\psi_\infty = 1$ allows us to form the ratio

$$\frac{|\hat{W}_{\text{obs}}|}{|\hat{W}_{\text{syn}}|} = \frac{\mu_s \psi_\infty}{\mu_{\text{inv}}} e^{-\gamma(\omega)r} \quad (3)$$

where μ_{inv} is the value of the shear modulus μ for the source layer obtained from the inversion. If the records are of high quality, then Equation (3) directly determines $\mu_s \psi_\infty$ and $\gamma(\omega)$ by using the fact that $\lim_{\omega \rightarrow 0} \gamma(\omega) = 0$.

Finally, the attenuation coefficients $\gamma(\omega)$ can be inverted to determine Q as a function of depth, at least in principle. In terms of the quality factors Q_α and Q_β of individual layers in the model, the attenuation coefficients may be written (Anderson, et al., 1965)

$$\gamma(\omega) = \frac{\omega}{2c^2} \left[\sum_{\ell=1}^N \frac{\partial c}{\partial \beta_\ell} \frac{\beta_\ell}{Q_{\beta_\ell}} + \sum_{\ell=1}^N \frac{\partial c}{\partial \alpha_\ell} \frac{\alpha_\ell}{Q_{\alpha_\ell}} \right] \quad (4)$$

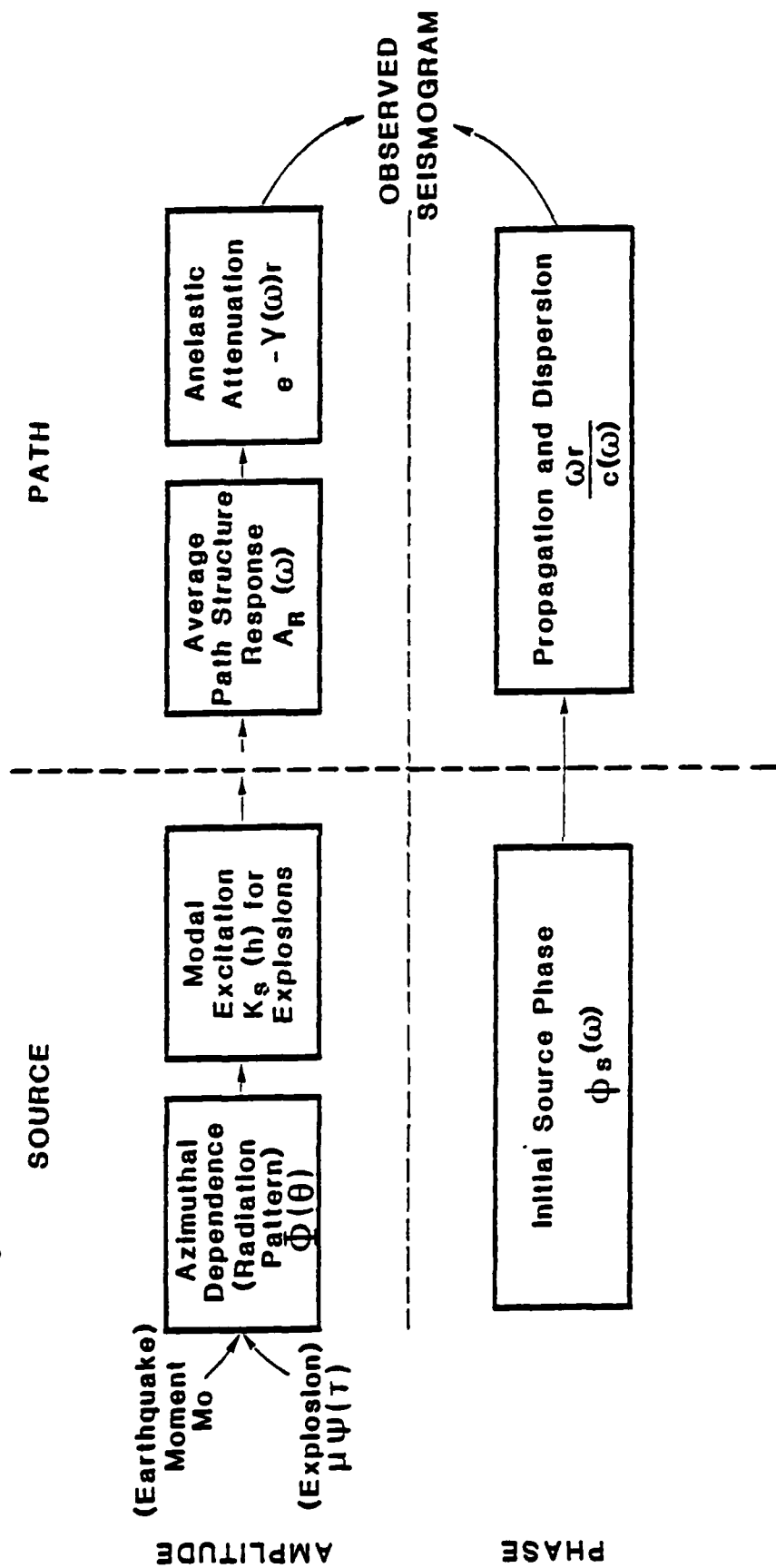


Figure 1. Major factors influencing surface wave spectra. The amplitude and phase factors are divided into source- and path-dependent features. A full path correction must determine the three features on the right of the diagram.

where the index l represents the layer number. The derivatives in Equation (4) are determined in the inverse calculation for earth structure. The phase velocity is largely insensitive to variations in α ; so the second sum is small compared to the first one. In addition, if all losses occur in shear, with no bulk attenuation, then $Q_\alpha \approx \frac{9}{4} Q_\beta$, which can be used as a constraint. Failure to obtain a physically reasonable model of attenuation structure is usually diagnostic of a complication in wave propagation (e.g., multipathing, lateral inhomogeneities) or in the recording (e.g., noise, faulty instrumentation), which has not been correctly identified in the analysis.

For seismograms which are too contaminated by noise to use Equation (3) for estimating $\gamma(\omega)$, we may still take attenuation into account, but the range of allowable Q models must be severely restricted, at the cost of achieving a less satisfactory fit to the observed seismogram. This procedure was adopted by Cheng and Mitchell (1981), who consider a one parameter family of Q models in their simultaneous analysis of several events with known moments.

The combined forward and inverse modeling used to obtain the path corrections is summarized in Figure 2 in the form of a flow diagram.

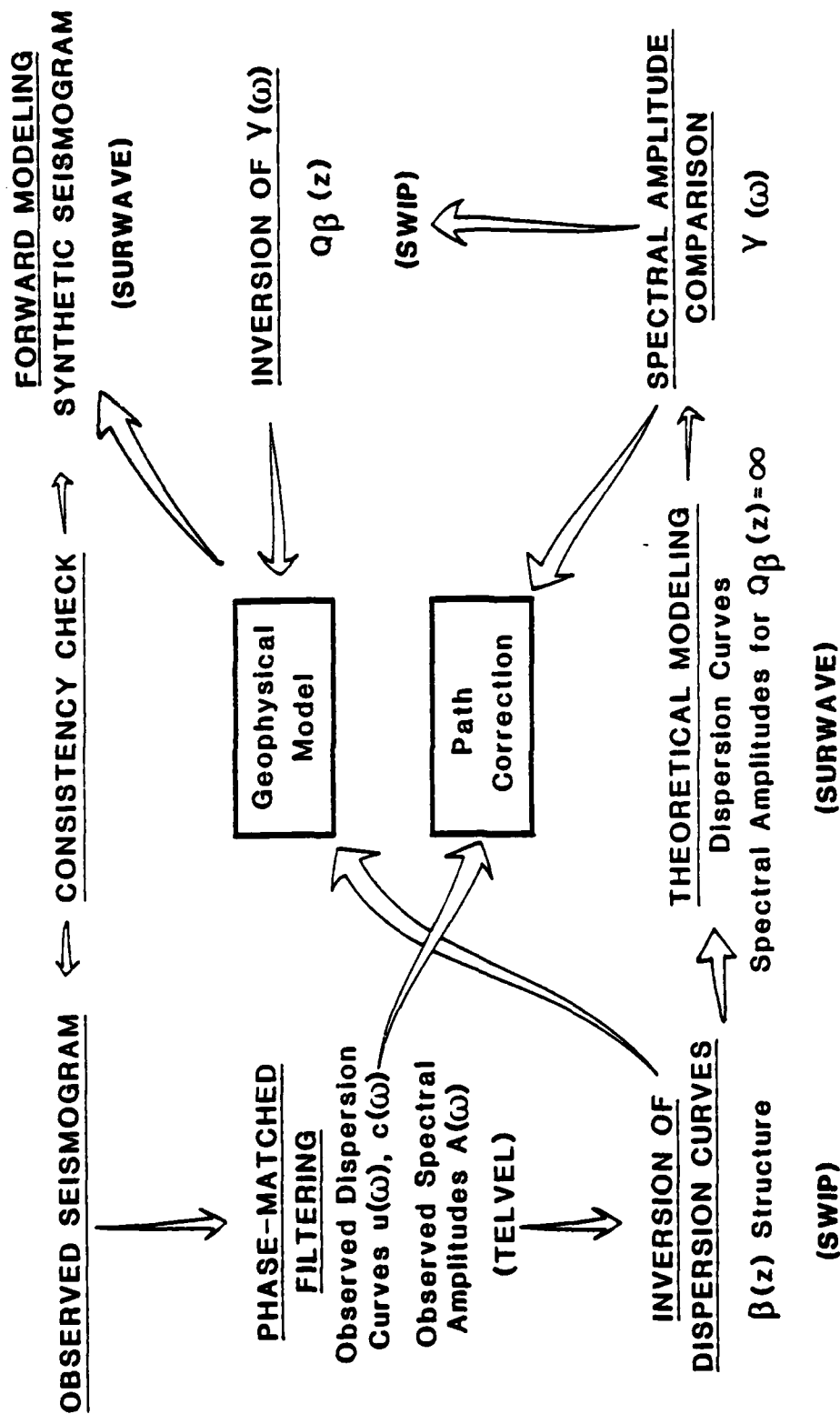


Figure 2. Flow diagram for determining path corrections. Dispersion curves and amplitudes are found by phase-matched filtering. Synthetic amplitudes from inverse structure are compared with observed amplitudes to estimate source amplitude and attenuation. Attenuation coefficients are constrained by and/or inverted for a Q model. The output is a geophysical model (velocity and Q structure) and the observed path effects (dispersion and attenuation).

III. PHASE-MATCHED FILTERING

The technique of phase-matched filtering for obtaining surface-wave dispersion and spectral amplitudes was first proposed by Herrin and Goforth (1977), although Dziewonski, et al. (1972) used essentially the same technique without iteration. Earlier methods included the graphical "peak and trough" method, narrow-band filtering (for example, Archambeau, Flinn and Lambert, 1966; Dziewonski, Block and Landisman, 1969), and moving-window analysis (Landisman, et al. 1968; Landisman, Dziewonski and Sato, 1969). Of these, the peak and trough method is simple, but rapidly becomes unreliable in the face of complications in the seismograms. Dziewonski, et al. (1972) demonstrate that the other two methods lead to systematic errors in the dispersion estimate whenever: (a) the amplitude spectrum $A(\omega)$ varies with frequency, and (b) the phase velocity $c(\omega)$ differs from the group velocity $u(\omega)$. Rarely, if ever, are these two conditions not satisfied.

The Herrin and Goforth method is based upon classical matched-filter principles. The basic idea is to remove as much dispersion from the seismogram as possible so that the resulting impulse-like signal becomes easy to process with conventional techniques.

Suppose a fundamental-mode surface wave $s(t)$ has a Fourier transform

$$S(\omega) = |S(\omega)| e^{ik(\omega)r} \quad . \quad (5)$$

The phase and group velocities are

$$c(\omega) = \frac{\omega}{k(\omega)} \quad (6)$$

$$u(\omega) = \frac{d\omega}{dk(\omega)} \quad . \quad (7)$$

We seek an estimate of $k(\omega)$. Suppose a known dispersion curve is specified by $k'(\omega)$:

$$S'(\omega) = |S'(\omega)| e^{ik'(\omega)r}. \quad (8)$$

The cross-spectrum of $S'(\omega)$ and $S(\omega)$ is given by

$$H(\omega) = S(\omega) S'^*(\omega) = |S(\omega)| |S'(\omega)| e^{i[k(\omega) - k'(\omega)]r} \quad (9)$$

where $*$ denotes complex conjugation. Ideally, if $k'(\omega) = k(\omega)$, the cross-correlation is phaseless (an even function). In addition, if $|S'(\omega)| = 1/|S(\omega)|$, then $|H(\omega)| = 1$ and $h(t)$ is an impulse. $S(\omega)$ is then the transfer function of a deconvolution or inverse filter. Alternatively, if $S'(\omega) = S(\omega)$, $H(\omega) = |S(\omega)|^2$ and $h(t)$ is the autocorrelation function of $s(t)$. The salient feature to note is that $H(\omega)$ has much less phase than $S(\omega)$, so that $h(t)$ is compressed in time with respect to $s(t)$.

The residual phase in $H(\omega)$ is small if $k'(\omega) \approx k(\omega)$, and consequently, the phase spectrum of $H(\omega)$ is much easier to unwrap compared to the phase spectrum of $S(\omega)$. If $\phi_h(\omega)$ is the phase spectrum of $H(\omega)$, then $k(\omega) = k'(\omega) + \phi_h(\omega)/r$.

Because $k'(\omega)$ is chosen to approximate $k(\omega)$, $S'(\omega)$ is called a phase-matched filter (PMF). The amplitude spectrum of $S'(\omega)$ can be arbitrarily chosen. The deconvolution filter $|S'(\omega)| = \frac{1}{|S(\omega)|}$ has good time resolution, but is extremely sensitive to extraneous noise. When $|S'(\omega)| = |S(\omega)|$, then $S'^*(\omega)$ is the classic matched filter which optimizes the signal-to-noise ratio in a least-squares sense. The resulting time resolution, however, is poor. A useful compromise between these extremes which the S^3 code utilizes is $|S'(\omega)| = 1$ so that $|H(\omega)| = |S(\omega)|$. Since the cross-spectrum preserves the amplitude spectrum of the observed seismogram, the PMF output spectrum yields noise-suppressed spectral amplitude estimates.

The greatest advantage of the phase-matched filtering approach stems from the time compression; it affords better noise rejection in spectral amplitude estimation and multipath separation. Both

these topics are well covered by Herrin and Goforth (1977), and will be only briefly mentioned here.

Since the filter is matched to the seismogram and not to the noise, the signal energy is compressed to times near $t = 0$ while the noise is not. Therefore, a spectral estimate of $h(t)$, evaluated from a time window near $t = 0$, is less contaminated by noise..

A multipathed, or a higher-mode arrival with group arrival time t_M will be time-shifted to $t = t_M - t_p$ where t_p is the primary group time, and not to $t = 0$. In addition, if the dispersion curve of the multipath does not match that of the primary, then the multipath component of the output signal will not be symmetrical. Herrin and Goforth give illustrative examples of these two effects.

Of critical concern is the resolving power of the PMF method; namely, how much time separation between primary and multipath arrivals is necessary to yield unperturbed dispersion curves and spectral amplitudes for the primary. The time width of the output $h(t)$ depends on the bandwidth of $|H(\omega)|$, which in turn depends upon the seismogram bandwidth. A larger bandwidth gives a narrower time domain signal, according to the uncertainty relation $\Delta t \Delta \omega \approx 1$. Our experience with synthetic data shows this to be the case.

The block diagram for the S^3 code TELVEL is shown in Figure 3. The algorithm is similar to that of Herrin and Goforth, except that the initial group velocity estimate is obtained by narrow-band filtering instead of being user-provided.

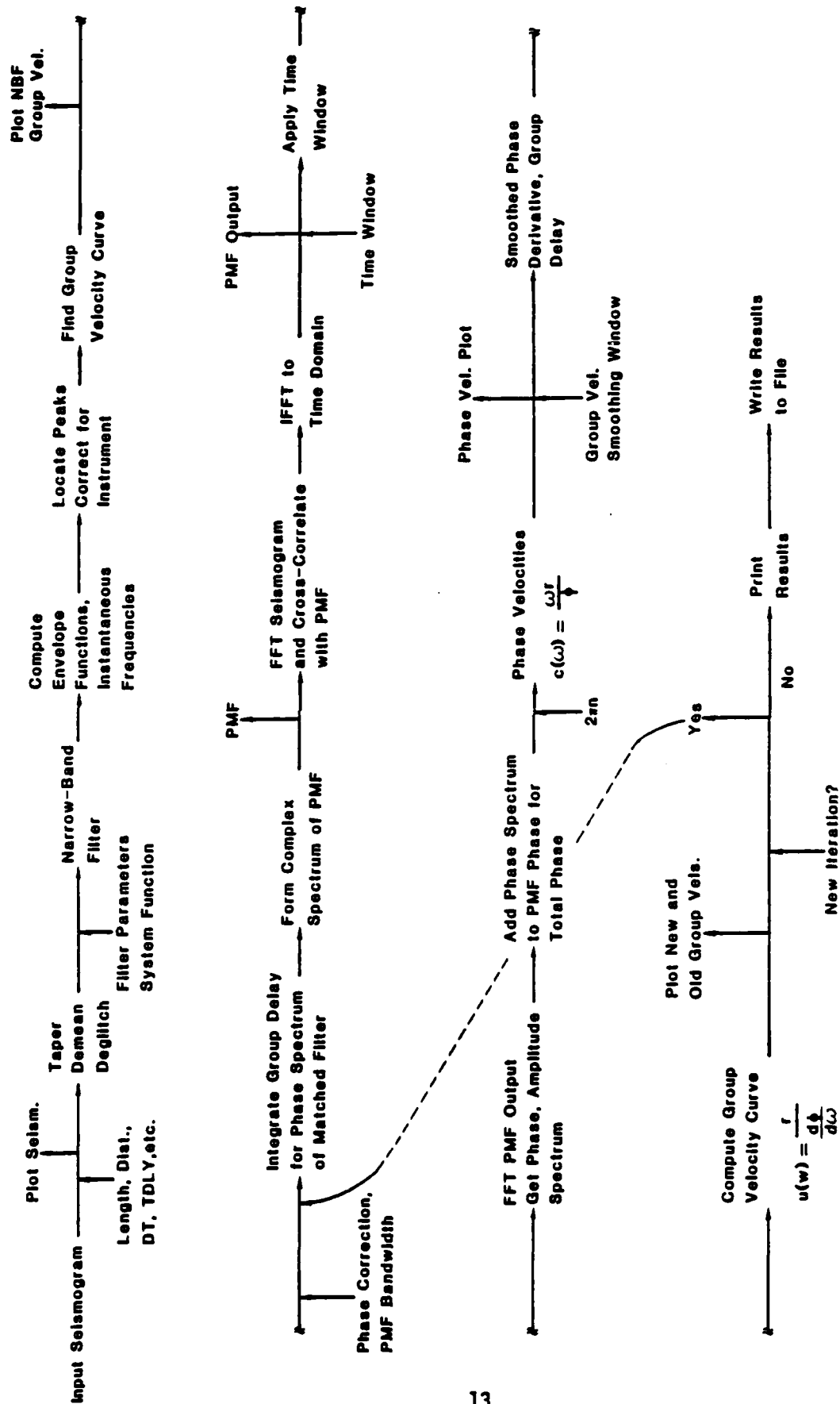


Figure 3. Block diagram, dispersion curve extraction. The program TELVEL uses phase-matched filtering as proposed by Herrin and Goforth (1977).

IV. TESTS OF PHASE-MATCHED FILTERING USING SYNTHETIC SEISMOGRAMS

Our tests with synthetic data started with the model and associated dispersion curves shown in Figure 4. Seismograms were generated for various epicentral distances and additively superposed to simulate multipathing (Figure 5). The source was an explosion at 800 meter depth with $\psi_{\infty} = 10^4 \text{ m}^3$.

As expected, TELVEL performed very well on synthetic S1, which involves no multipathing, and on synthetic S2, which has well-separated groups. Typical phase velocity errors were within $\pm 0.002 \text{ km/sec}$, and typical group velocity errors within $\pm 0.004 \text{ km/sec}$ in the 5-200 sec band. Greater group velocity errors are to be expected because of the derivative operation (Equation 7). Figure 6 shows the clean separation of arrivals achieved for synthetic S2.

Test case S3 is at the limit of resolution of the phase matched filter method. The first two arrivals could not be clearly separated. Nevertheless, S3 yielded good phase velocities (errors $< \pm 0.005 \text{ km/sec}$) in a limited period range of 5.3 to 40.0 seconds. Group velocity errors were about $\pm 0.010 \text{ km/sec}$ from 5.7 to 25.0 seconds.

Interference of the closely spaced arrivals in S4 made it impossible to obtain a dispersion curve at all for this seismogram. Individual arrivals could not be resolved using either phase-matched filtering, or narrow-band filtering. Even in this extreme case, however, the complexity of the seismogram did not lead to an incorrect dispersion curve; it was simply impossible to obtain any dispersion curve.

Synthetic S5 was the only one in this series where higher modes were included. The analysis of this seismogram presented no difficulty — probably because the higher modes were of low amplitude and distinct from the primary arrival in both frequency and time. Errors were comparable to those obtained with S1 and S2. These tests on synthetic seismograms show that the PMF method is an accurate and stable way of finding dispersion curves.

EASTERN US

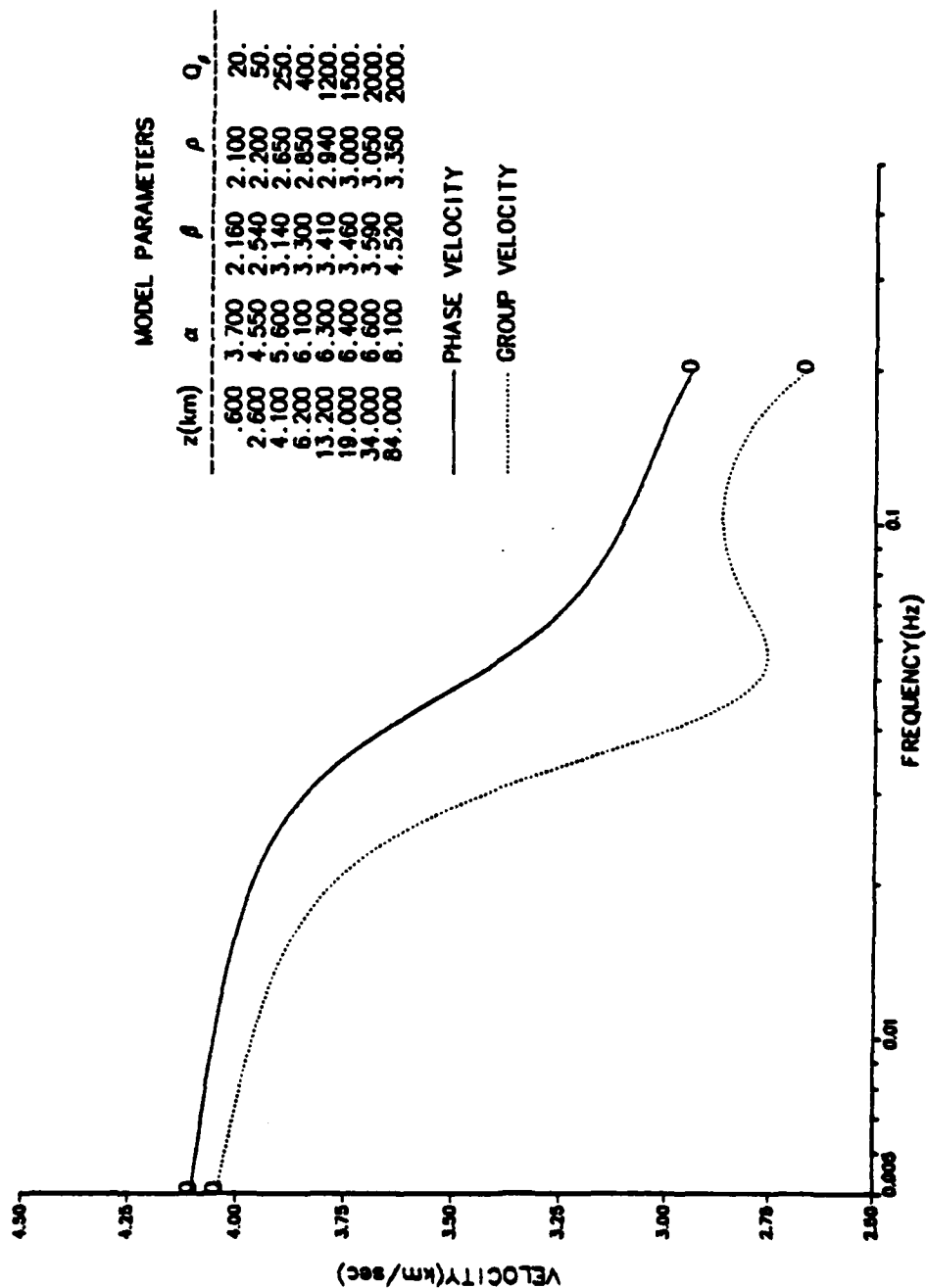


Figure 4. Eastern United States structure and Rayleigh fundamental-mode dispersion waves. The structure is model S1 of Bache, Swanger and Skholter (1980).

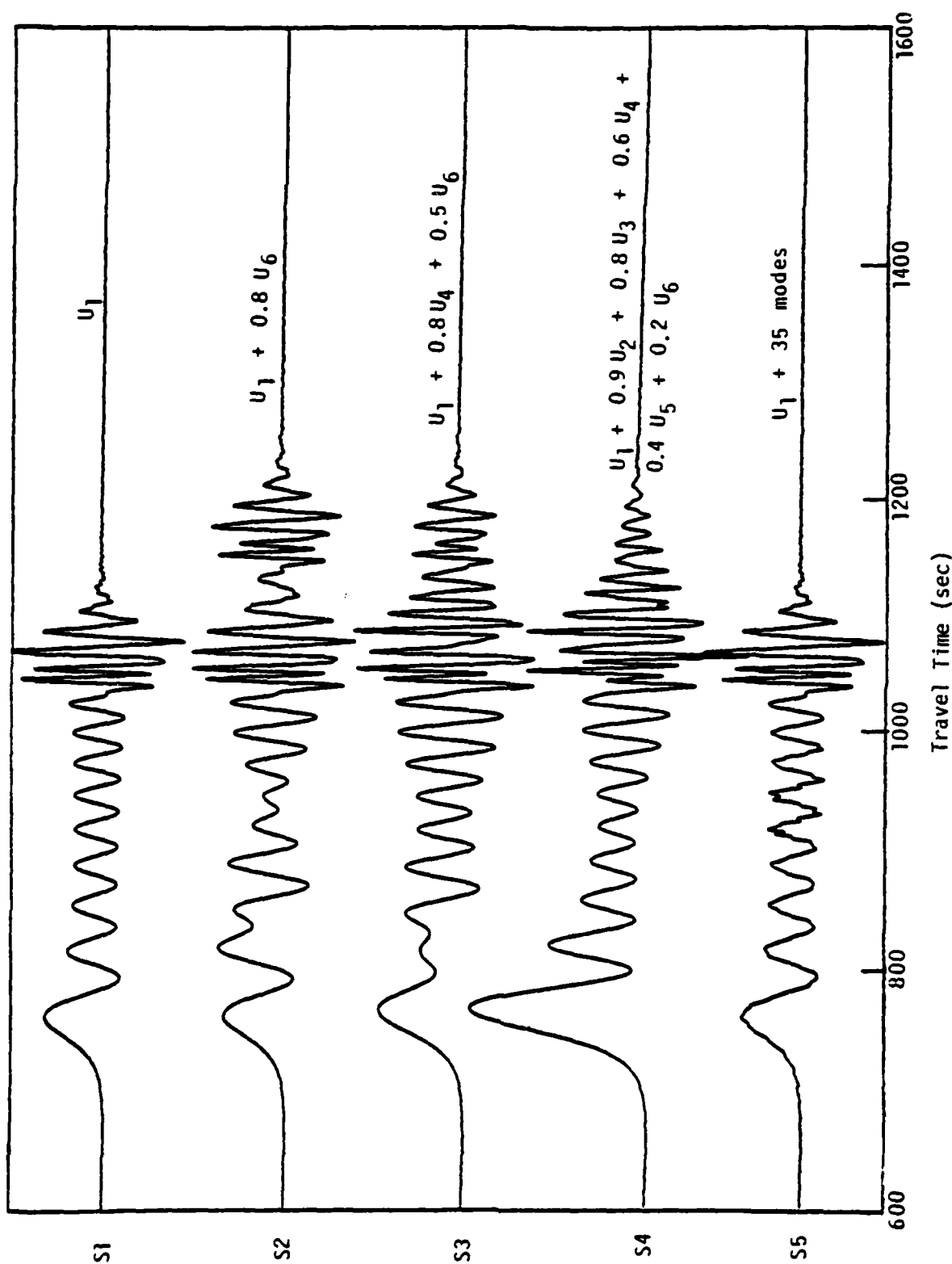


Figure 5. Synthetic seismograms from Eastern United States structure. Fundamental mode, vertical-component Rayleigh waves at the following distances were computed: U_1 , 3000 km; U_2 , 3020 km; U_3 , 3050 km; U_4 , 3100 km; U_5 , 3200 km; U_6 , 3300 km. The seismograms were then additively combined to produce the simulated multipathed signals 2, 3 and 4. Neither S1 nor S5 contain multipaths; S1 is fundamental-mode only, and S5 contains 35 higher-order modes.

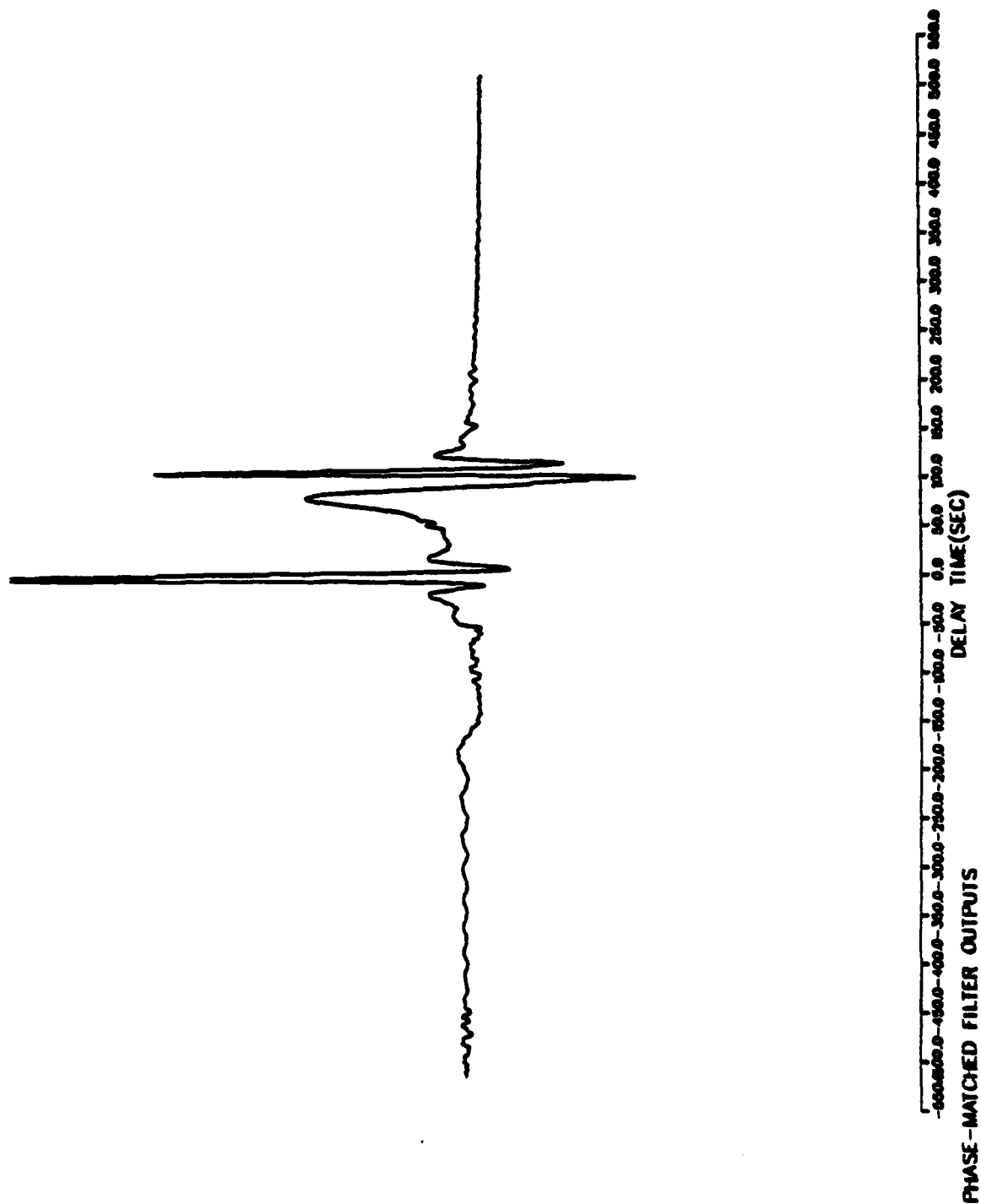


Figure 6. PMF output for S2. The two sharp pulses represent the two separate arrivals. The second pulse is asymmetrical because the PMF is matched only to the dispersion of the primary arrival.

It should be noted in the foregoing discussion that single-station phase measurements are ambiguous with respect to additive multiples of $\pm 2\pi n$, since

$$|S(\omega)|e^{ikr} = |S(\omega)|e^{i[k \pm \frac{2n\pi}{r}]r} \quad (10)$$

The correct value of n can be found if:

1. The phase velocity at one frequency is known;
2. The data extends to low enough frequency so that the fact that $\lim_{\omega \rightarrow 0} k(\omega)r = 0$ can be exploited;
3. Multiple station data of proper spacing and bandwidth are available.

An improper value of n affects the phase velocity estimates (particularly at low frequencies since $c = \frac{\omega r}{\phi \pm 2n\pi}$) but does not effect group velocity estimates (Equation 7).

V. STRUCTURE INVERSION - TEST ON SYNTHETIC DATA

The observed dispersion curves can be systematically inverted to infer the average earth structure along the path of travel. Although the relation between dispersion and structure is nonlinear, the problem can be linearized and a best-fit solution to the data approached by successive iterations. This method was used successfully by Bache, et al. (1978) to infer crustal structure in the southwestern United States. The method may also be adapted to infer $Q_\beta(z)$.

The procedure assumes that the entire travel path from source to receiver can be adequately represented by a plane layered earth structure. It yields estimates $\hat{\alpha}(z)$, $\hat{\beta}(z)$, and $\hat{\rho}(z)$ corresponding to average values of these quantities over the path. In addition, the corresponding resolving kernels are computed and characterized by a simple measure of spread. In practice, $c(\omega)$ and $u(\omega)$ do not permit estimation of $\alpha(z)$ and $\rho(z)$ independently of $\beta(z)$. There are, however, good geophysical arguments for constraining α and ρ to be linear functions of β :

$$\hat{\alpha}(z) = C_{1\alpha}(z) \hat{\beta}(z) + C_{2\alpha} \quad (11a)$$

$$\hat{\rho}(z) = C_{1\rho}(z) \hat{\beta}(z) + C_{2\rho} \quad (11b)$$

In other words, we assume that a Birch-type law holds in each layer, and fix Poisson's ratio at each depth. Dobrin (1976, page 53) shows empirical evidence supporting these assumptions.

The basic requirement imposed on a model is that it should fit the data. However, measurement errors, as well as the finiteness of the data set, lead to well-known difficulties and often to unstable or geophysically implausible solutions. In order to ensure stability as well as smoothness of the solution, the quantity

$$(\text{r.m.s. misfit})^2 + \epsilon (\text{model norm})^2$$

is, in fact, minimized. The model norm is defined by

$$\int_0^{\infty} dz \left[\frac{d\beta}{dz} \right]^2$$

so that a smoother model possesses a smaller norm. ϵ parameterizes the inevitable tradeoff between these two terms, which is illustrated on Figure 7 in the form of a "tradeoff curve."

Inversion theory as applied in this report is discussed by Wiggins (1972), Jackson (1972), and Jordan (1972).

The optimal point on the tradeoff curve is defined as the point for which neither r.m.s. misfit nor model norm are too large. Typically, one chooses a value of ϵ corresponding to the point on the curve closest to the origin. ($\epsilon \sim 100$ on Figure 7).

Other features of our inversion program include:

1. The capability to impose local constraints such as fixing the velocities at discrete depth points.
2. The possibility of introducing discontinuities at selected depths (e.g., Moho, or sedimentary layer if high frequency data are available).

The next step in our synthetic test was to invert the dispersion data obtained from S1 (Figure 8). This test was a "blind" one in that the operator did not know the "real" structure. The inversion model shown in Figure 8 incorporated no discontinuities, and no fixed data points were entered. The near surface layers are not resolved due to the lack of short period ($T < 5$ second) dispersion data.

The steep rise in $\beta(z)$ in the 20-45 km region is evidence of a discontinuity that is smoothed by the inversion. The next inversion run incorporated a discontinuity at the midpoint of this region, which, in fact, coincided with the "real" crust/mantle interface

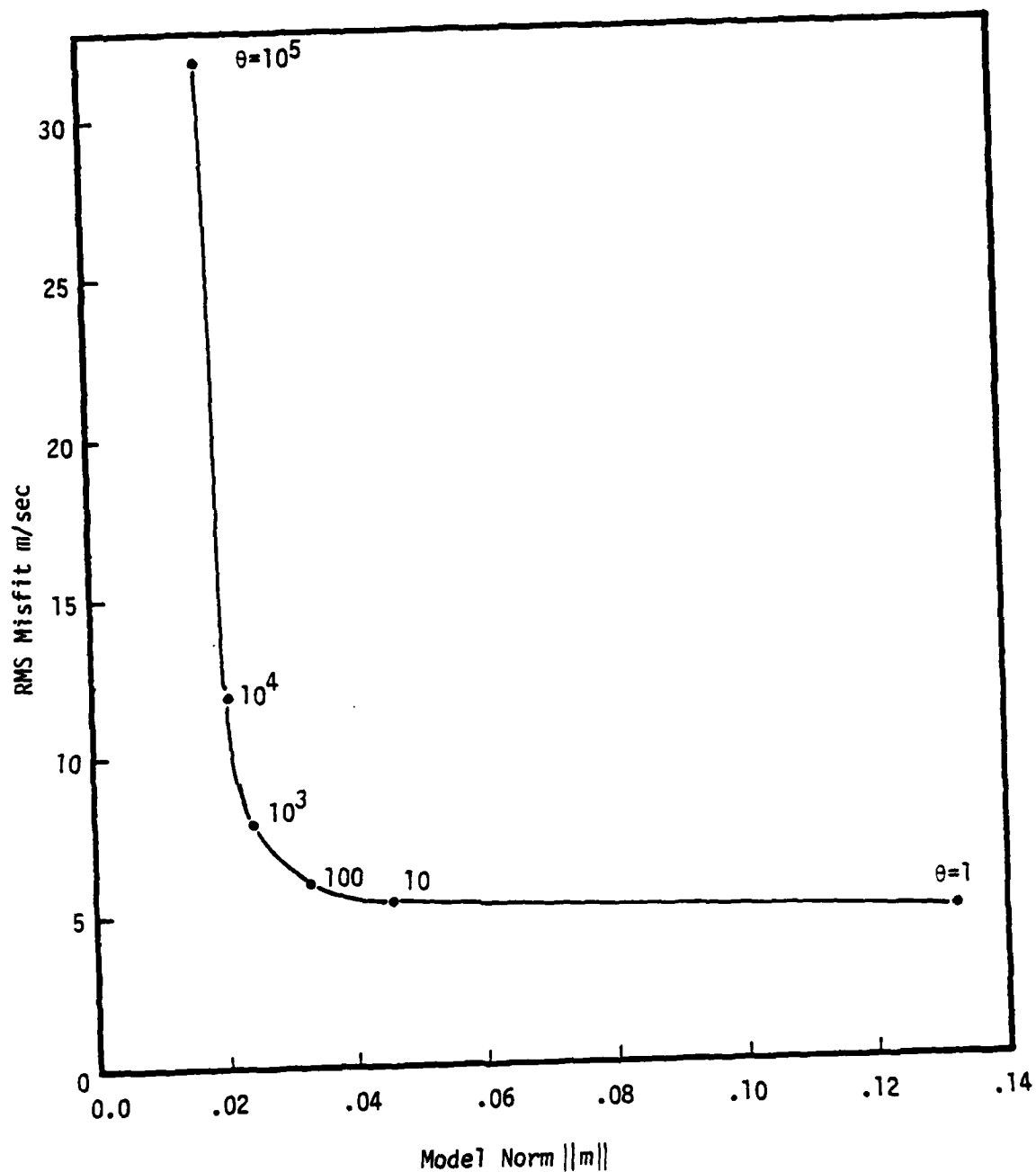


Figure 7. Tradeoff curve. The RMS fit of the model to the observed data is plotted against the model norm for various values of the tradeoff parameter θ . For high θ , the model is smooth ($\partial\beta/\partial z$ nearly constant) but the data fit is poor.

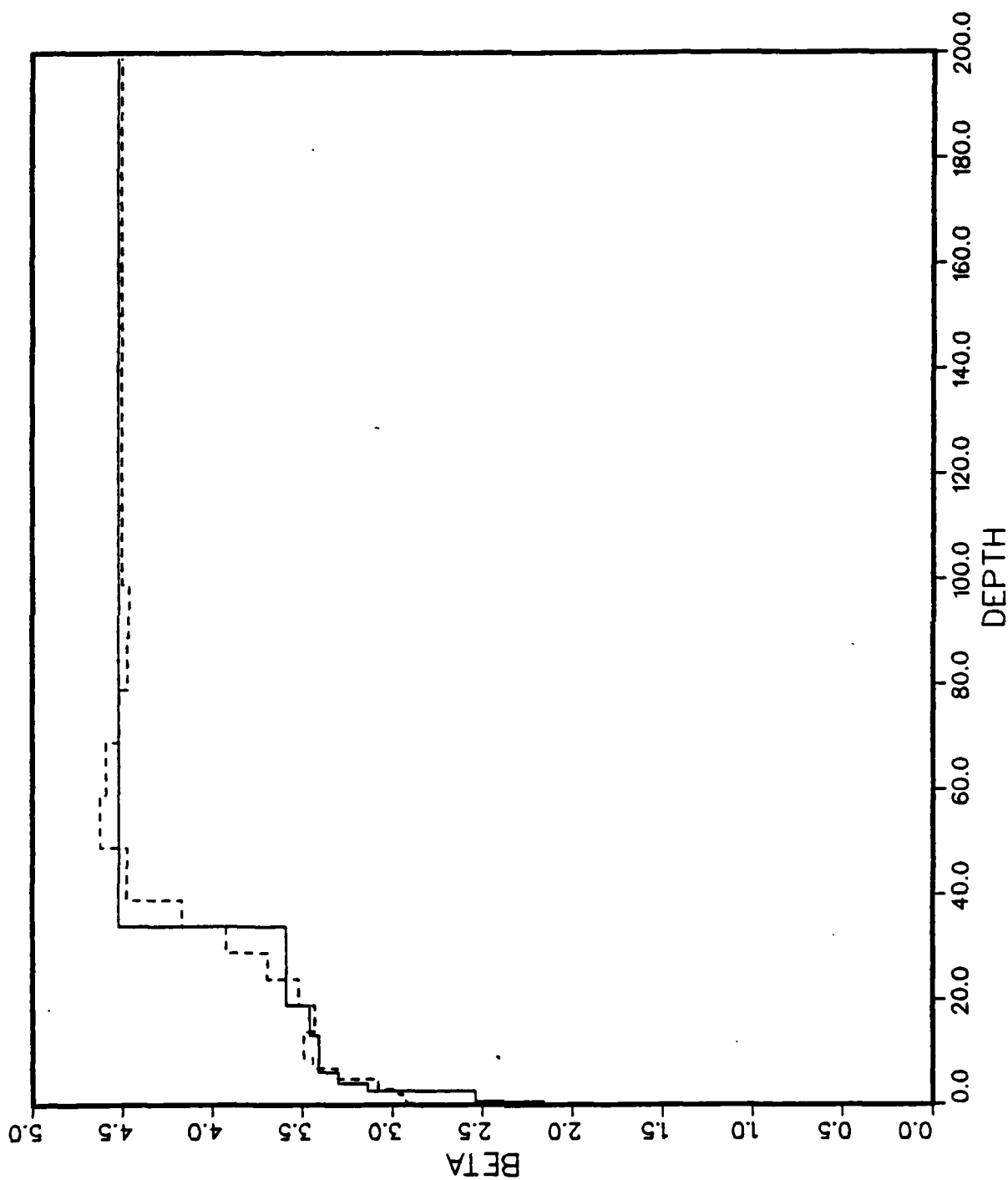


Figure 8. Inversion model #1, no crust/mantle discontinuity. The actual model is shown as a solid line; the inverted model as a dotted line. The steep gradient between 30 and 40 km is symptomatic of a discontinuity mollified by the smoothness criterion.

(Figure 9). The accuracy of this inversion is remarkable. When compared to the real model, the inversion used a Birch's Law that was significantly different from that used to generate the synthetic seismograms.

Inversion (After Dobrin)	Eastern United States (Bache and Swanger, 1980)
Crust $\rho = 0.22\beta + 1.9$	$\rho = 0.82\beta + 0.12$
Mantle $\rho = 0.65\beta + 0.4$	$\rho = 0.65\beta + 0.4$

To fully illustrate the capabilities of the procedure, we ran a third inversion with the "true" relations. In all cases, Poisson's ratio was fixed at 0.27 ($\alpha = 1.80\beta$). This last calculation gave a very accurate model, except for the near-surface sedimentary layers (Figure 10).

Although different in structure, the three models presented all fit the data well. R.M.S. misfits to the observed dispersion curves were 0.006 km/sec in all three cases (Figure 11); so, on the basis of the data alone, the three models are equally good. However, without knowledge of the "true" structure, we would have chosen the second inversion (Figure 9) because it contains a crust/mantle structure, and it satisfies empirical density-velocity relations discussed in the literature (e.g., Dobrin).

The dispersion data included observations every 0.005 Hz from 0.005 Hz to 0.20 Hz for both $c(\omega)$ and $u(\omega)$. The variance estimates and resolution of the inversion model are summarized below in terms of standard deviations of the estimated parameters and spreads of the resolution kernels.

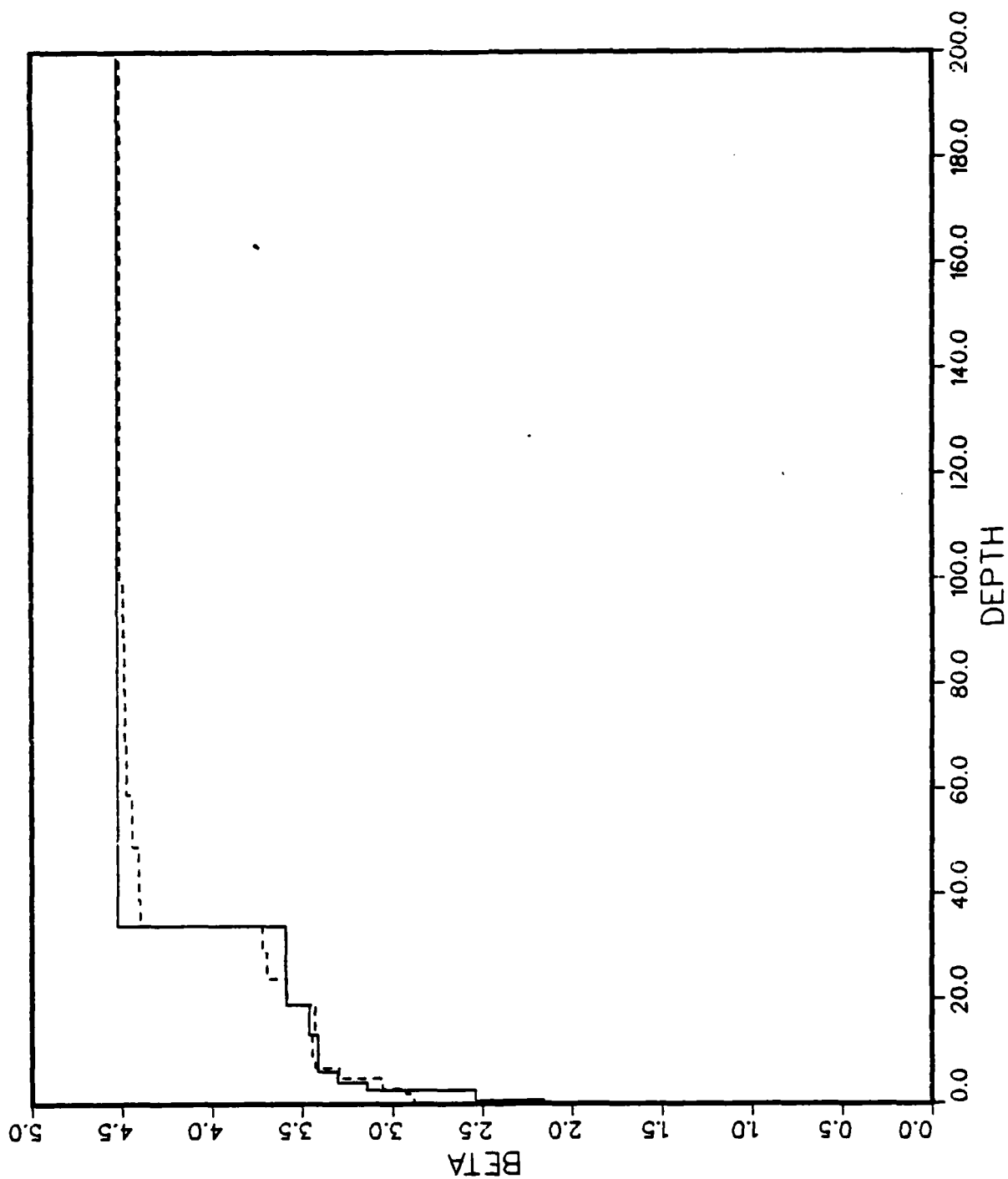


Figure 9. Inversion model #2, discontinuity at 34 km. On the basis of Model #1 (Figure 8), a discontinuity was inserted in the inversion model at 34 km.

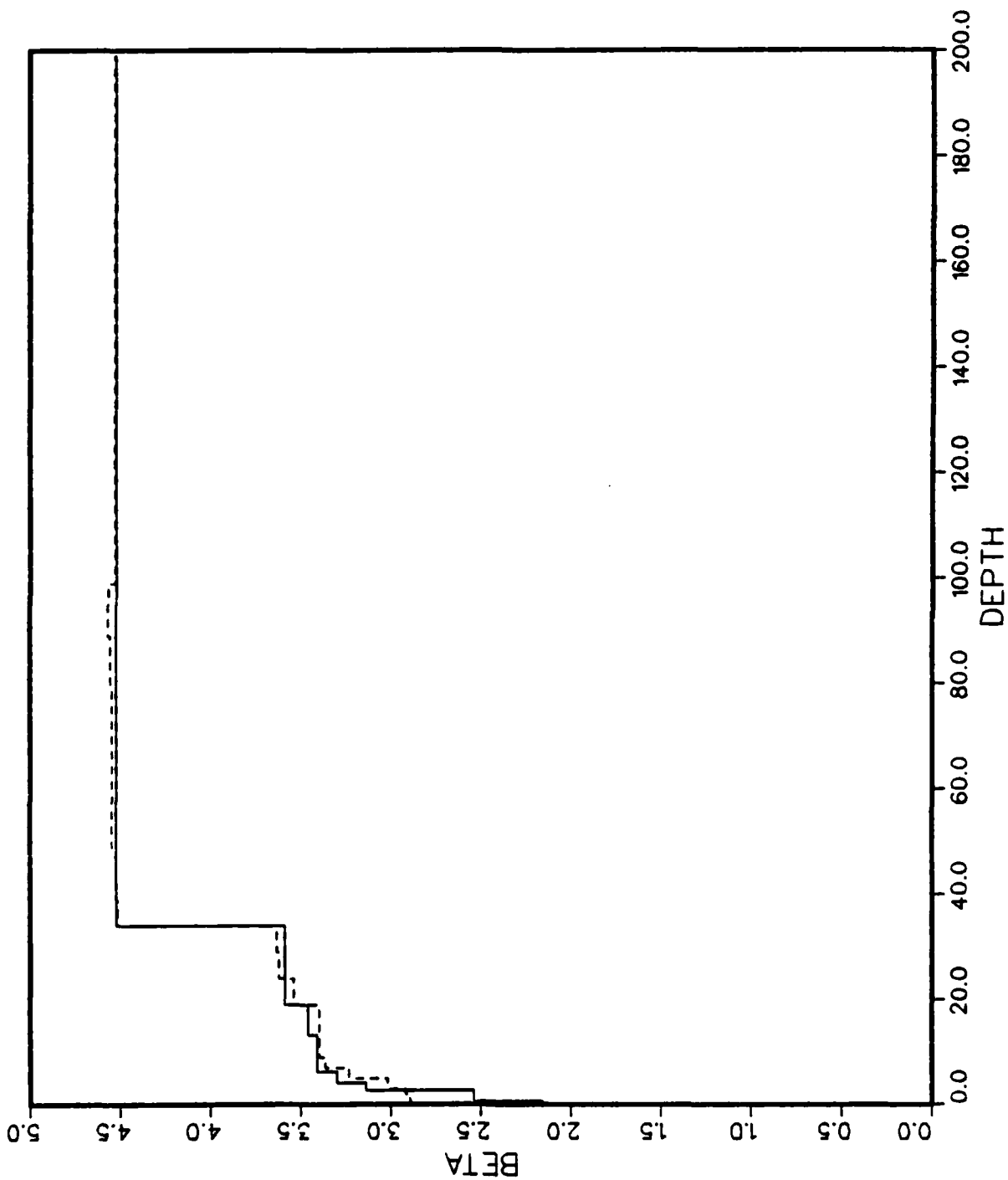


Figure 10. Inversion model #3, in which the known $\rho(\beta)$ relation is used. This inversion was run to show the capabilities of the inversion procedure. Normally, the $\rho(\beta)$ relation in a given region is not known, and global average values must be used as in Model #2.

MODEL PARAMETERS

z(km)	α	β	ρ	Q_p
500	5.174	2.874	2.532	81.
1.000	5.182	2.879	2.533	81.
2.000	5.198	2.888	2.535	81.
3.000	5.267	2.926	2.544	82.
5.000	5.496	3.053	2.572	86.
7.000	5.928	3.293	2.625	93.
9.000	6.169	3.427	2.654	97.
14.000	6.197	3.443	2.657	97.
19.000	6.165	3.425	2.653	96.
24.000	6.452	3.584	2.689	94.
29.000	6.646	3.692	2.712	97.
34.000	6.696	3.720	2.718	98.
39.000	7.914	4.396	3.258	116.
49.000	7.927	4.404	3.263	95.
59.000	7.996	4.442	3.287	97.
69.000	8.046	4.470	3.306	99.
79.000	8.067	4.482	3.313	100.
89.000	8.075	4.486	3.316	102.
99.000	8.080	4.489	3.318	103.
199.000	8.116	4.509	3.331	102.

PL1C1 DISPERSION

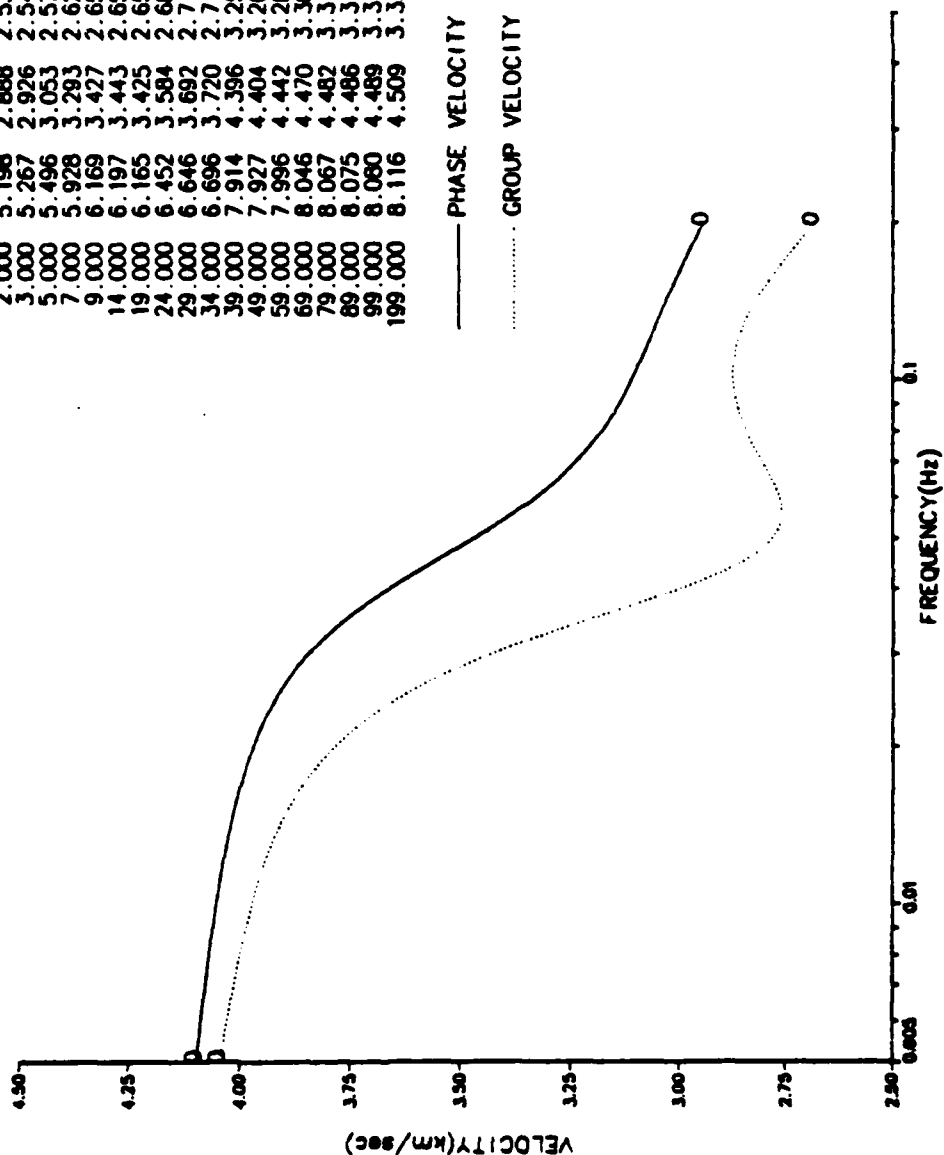


Figure 11. Dispersion curves from inversion model #2. These curves should be compared to those in Figure 4. The RMS misfit is 0.006 km/sec.

DEPTH (km)	NUMBER OF LAYERS	STANDARD DEVIATION (m/sec)	SPREAD (km)
0-3	4	11-15	13-25
3-19	5	5-8	4-11
19-34	3	10-15	11-27
34-99	7	15-20	20-40
99-199	1	3	---

The structure is best resolved in the 3-19 km range. Both the standard deviations and the spread gradually increase below this depth. The single bottom layer is well-resolved because of the inclusion of long-period phase velocity data, but the spread is not defined for this layer. The near surface layers have spread greater than depth, an indication of insufficient information content in the data (in this case, lack of high frequency data).

The frequency range that was obtained from the synthetic seismograms is optimistic for actual data. A typical range is 0.02 Hz - 0.12 Hz (50-8 sec). The loss of long-period data reduces the maximum resolvable depth, and such a restriction would probably limit an accurate model to the crust and very top of the mantle. However, the good resolution obtained at mid-crustal depths would be retained.

Another problem can arise because of the $\pm 2n\pi$ phase ambiguity discussed earlier. The result of choosing an incorrect value of n will cause the velocities of the lower layers to be incorrect. The velocities of the upper layers are more strongly constrained by the group velocity than the phase velocity, and so are little affected.

VI. ATTENUATION, MOMENT ESTIMATES AND INVERSION FOR Q STRUCTURE

Once the inverse structure has been determined, synthetic spectral amplitudes can be computed and used to estimate the long period source level $\mu\psi_\infty$ and the attenuation coefficients $\gamma(\omega)$. The synthetic test seismograms, of course, simulate the ideal data set and therefore produce the best estimates of attenuation and source level that we can hope to obtain.

For the synthetic test, we used inversion model 2 (Figure 9) for computation of inverse synthetic seismograms. At the longest usable period of 200 seconds, we set $\gamma(\omega) = 0$. With this constraint, both the source level and $\gamma(\omega)$ are determined. The estimated value of $\mu\psi_\infty$ differed from the true value by less than 2 percent. A comparison of the "true" $\gamma(\omega)$ with the estimated $\gamma(\omega)$ is shown in Table 1.

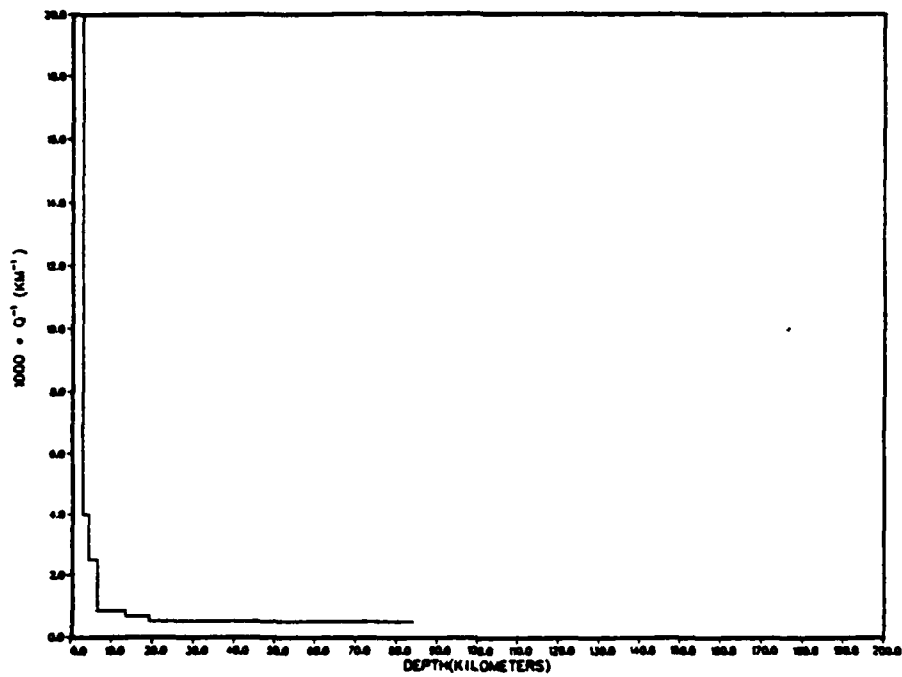
In order to assess the accuracy of the attenuation coefficients, we inverted them (see Equation (4)) in terms of a $Q_B(z)$ model (Figure 12). The inverted Q model is a good approximation to the "true" Q structure. The sharp discontinuity in Q at shallow depths has, of course, been smoothed by the inversion procedure.

TABLE 1

ACTUAL AND ESTIMATED ATTENUATION COEFFICIENTS

<u>Period</u>	<u>γ Estimated ($10^{-4}/\text{km}$)</u>	<u>γ True ($10^{-4}/\text{km}$)</u>
200	0.00	0.02
100	0.03	0.05
50	0.15	0.12
40	0.22	0.18
30	0.35	0.31
25	0.49	0.47
20	0.77	0.79
15	1.26	1.41
10	2.47	2.91
5	10.60	11.70

EASTERN US ITER = 1



PLIC1 Q-INVERT ITER = 2

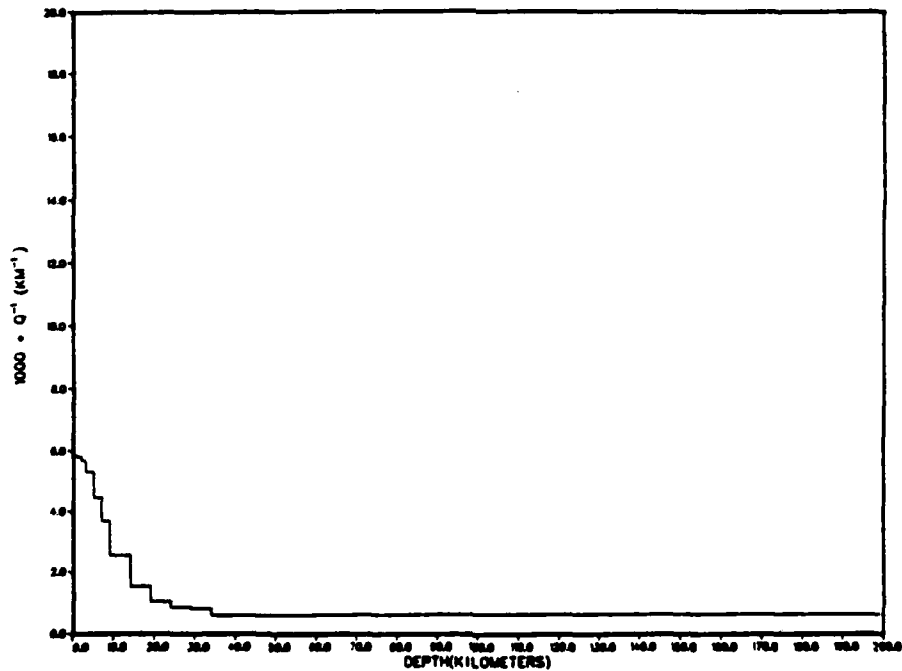


Figure 12. Inverted Q-model (bottom) and actual Q-model (top).

VII. TEST USING HOGGAR DATA

Surface wave recordings of the French Sahara event SAPHIRE (27 February 1965) were used to test the S^3 surface wave codes. The recordings were from two WSSN stations, Shirez, Iran (SHI) and Addis Ababa, Ethiopia (AAE). These seismograms were manually digitized from film-chip reproductions (Figure 13).

These two seismograms are a subset of a larger data set processed by Rodi, et al. (1978). In that study, dispersion curves and velocity structures were derived. However, dispersion curves were found by narrow-band filtering rather than phase-matched filtering and no attempt was made to perform an inversion for $Q_p(z)$. The results shown in this report were found independently of the work of Rodi, et al. (1978).

The SHI seismogram (Figure 13a) shows fairly clean dispersion, little evidence of higher modes, and moderate background noise. A multiple arrival is evident at about 1740 seconds. Since this arrival is not clearly separated from the primary, it caused a slight perturbation from a smooth group velocity curve.

The AAE seismogram (Figure 13b) shows two unusual features: significant inverse dispersion (high frequencies arrive first), and a "boxcar"-like amplitude envelope. Background noise and possibly higher modes and multipaths are present.

The velocity structures inverted from the two seismograms both show a smooth gradient from surface to mantle and have no definite manifestations of a crust/mantle discontinuity (Figure 14). However, the average near-surface velocity for the SHI path is much lower than that for the AAE path.

The comparison of observed and synthetic spectral amplitudes for attenuation estimates led to several difficulties. Most notably, the AAE spectrum peaked at intermediate periods, and so

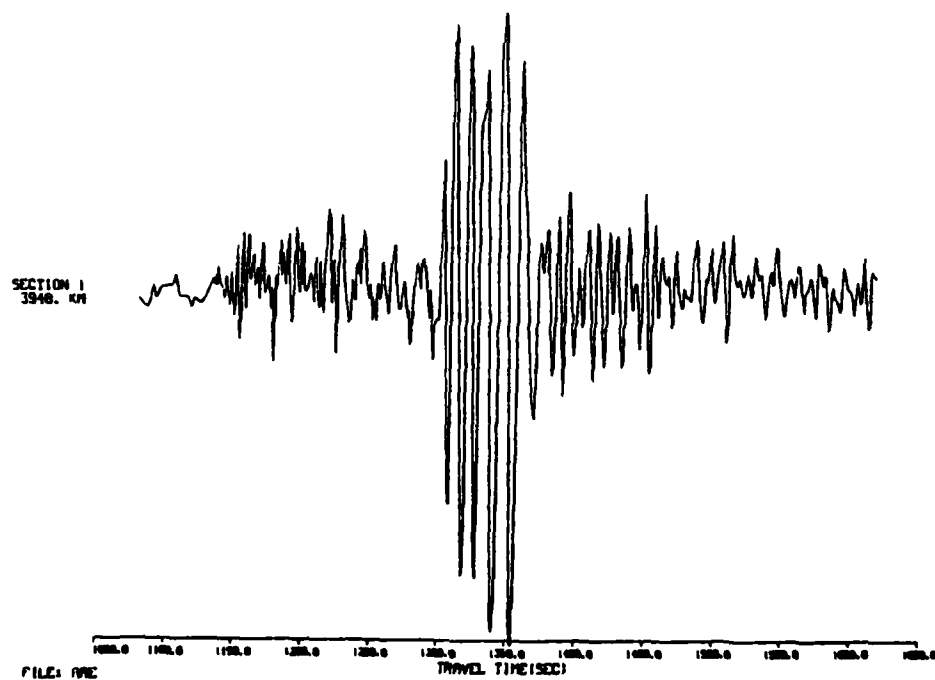
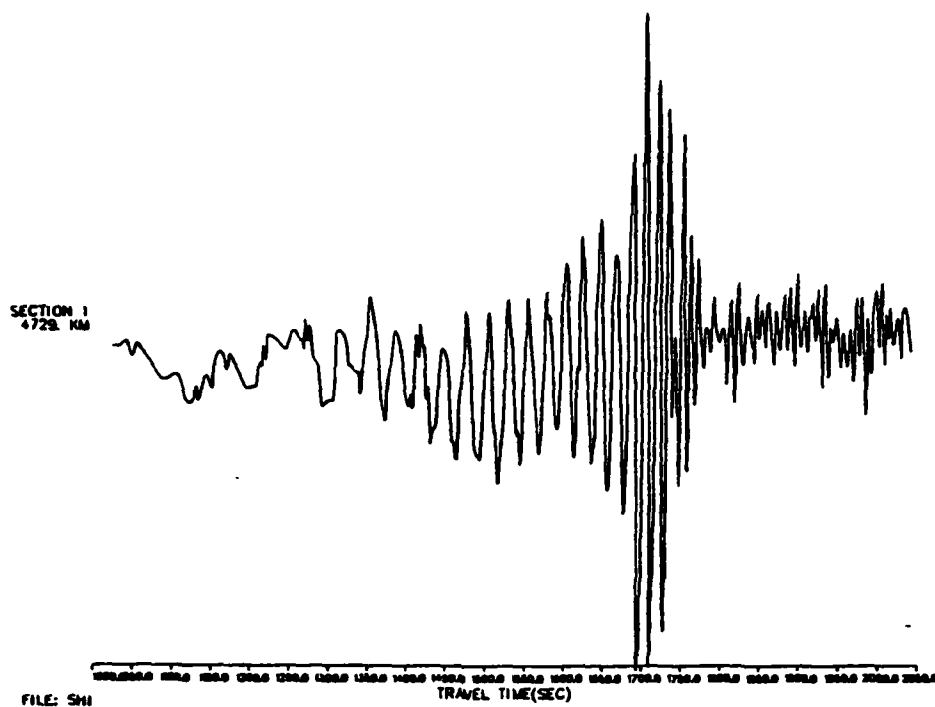
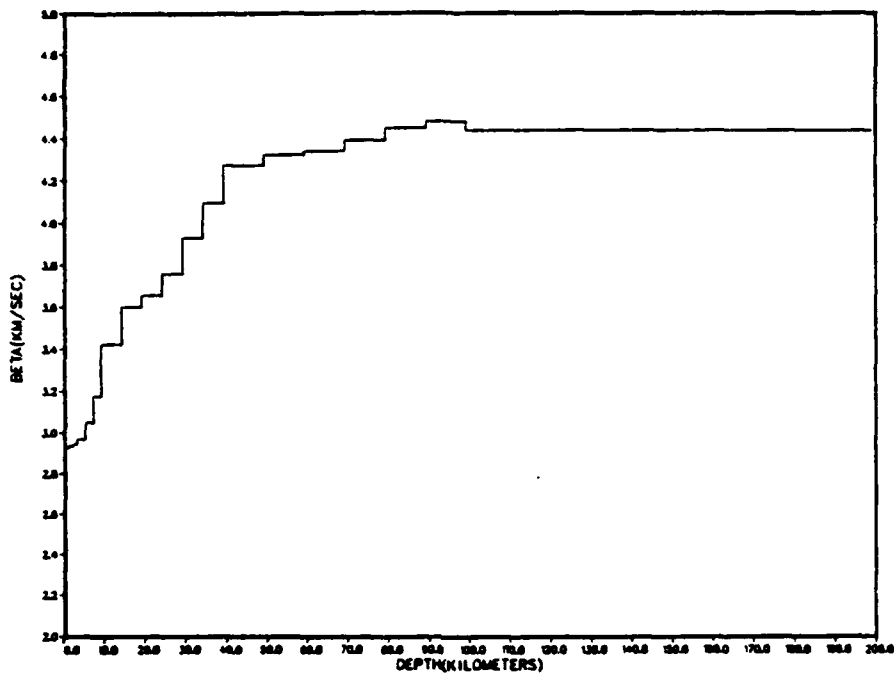


Figure 13. Surface waves from SAPHIRE, February 1965, at Shiraz, Iran (SHI), 4729 km (top), and Addis Ababa, Ethiopia (AAE), 3948 km (bottom).

HOG-SHI C,U ITER = 4



HOG-AAE C,U ITER = 4

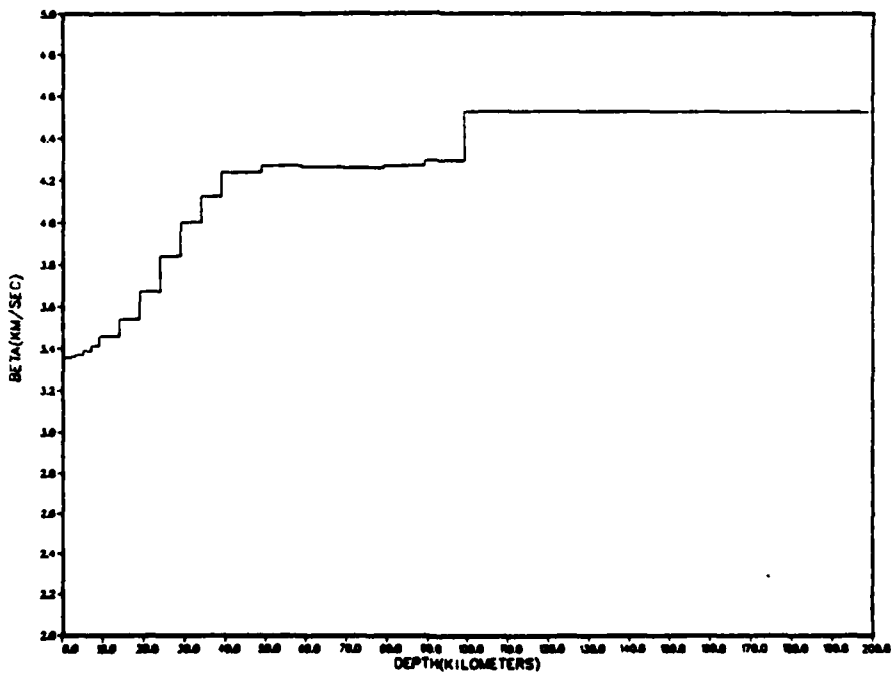


Figure 14. Inverted velocity-structures from SAPHIRE seismograms: (a) SHI, (b) AAE.

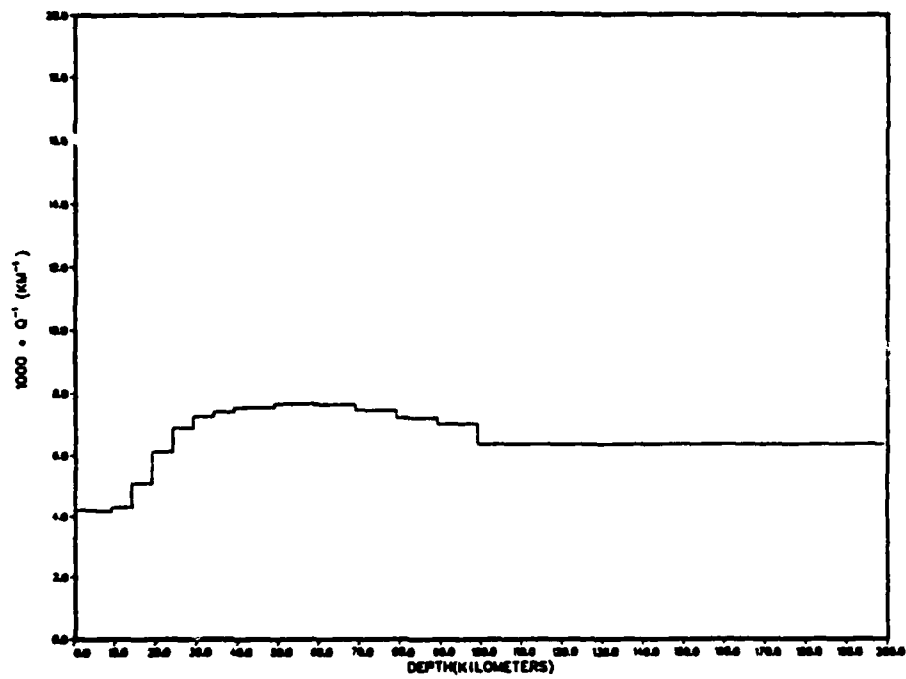
constraining $\gamma(\omega) = 0$ at the longest period would have resulted in negative apparent attenuation at shorter periods. We then changed our constraint so that $\gamma(\omega)$ is positive for all frequencies.

The resulting $Q_\beta(z)$ structures are shown in Figure 15. The models are quite different in spite of the fact that the paths differ in azimuth by only 35 degrees. Needless to say, we can only express low confidence in these results. The observed/synthetic spectral amplitude ratio showed differences that are too great to be attributed to simple attenuation, and the inverted $Q_\beta(z)$ structures are implausible. Nevertheless, the synthetic seismograms resulting from the inverted $\beta(z)$ and $Q_\beta(z)$ structures generally match the actual seismograms quite well (Figure 16). The peak amplitude for SHI is about one cycle too late, probably due to difficulties in measuring the dispersion curve near the Airy phase. Note that the suspected multiple arrival mentioned earlier is not present in the synthetic.

Background noise is likely to be a major contributing factor in the observed errors, particularly since the data was hand-digitized. However, we suspect that an even more serious problem arises from lateral variations in structure along the path. No reasonable plane-layered model would accurately replicate the observed spectrum. It is quite likely that a simple plane-layered model is inadequate when the path involves complex tectonic features. In our examples, station SHI is near the Zagros Suture Zone, while station AAE is in close proximity to the East Africa Rift Zone.

Our current work is focused on identifying such problems and implementing appropriate improvements to the basic algorithms.

HOG-SHI Q-INV #1 ITER = 2



HOG-AAE Q-INV # ITER = 2

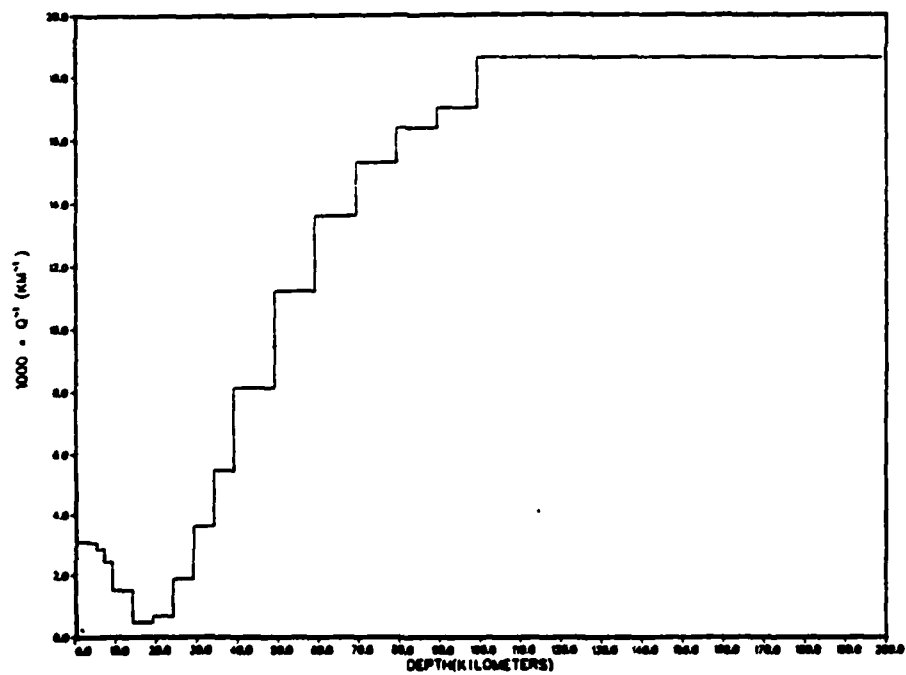


Figure 15. Inverted $Q_{\beta}(z)$ structures from SAPHIRE seismograms: (a) SHI, (b) AAE.

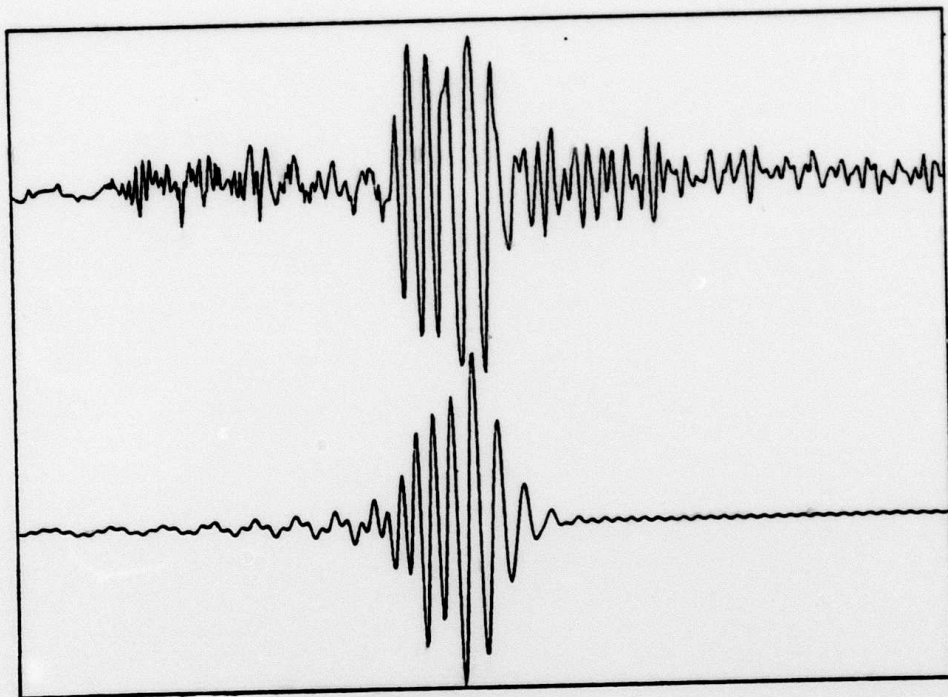
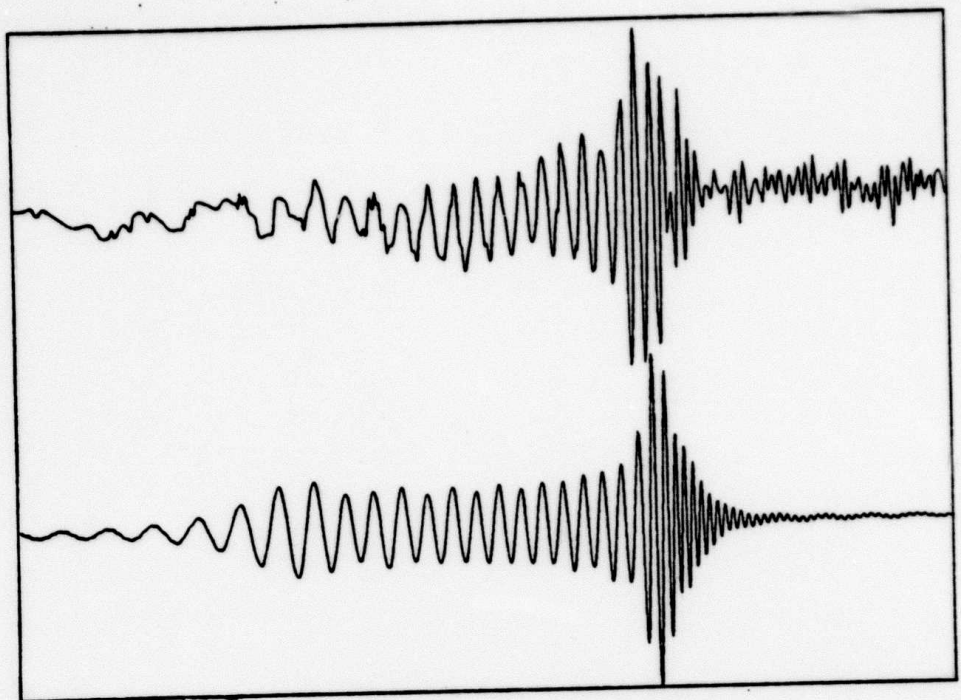


Figure 16. Actual seismograms (top) compared with synthetic seismograms computed from inverted $\beta(z)$ and $Q_{\beta}(z)$ models (bottom): (a) SHI, (b) AAE.

VIII. COMPUTER CODES

The S^3 surface wave processing is broken down into three separate programs: TELVEL, for computing dispersion curves and spectral amplitudes; SWIP, for inverting dispersion curves and $\gamma(\omega)$ for $\beta(z)$ and $Q_\beta(z)$; and SURWAV, for generating synthetic seismograms (Figure 2).

TELVEL is an interactive program with graphics designed to work on a Tektronix 4014 CRT storage terminal. Operator interaction is necessary to recognize multipath arrivals and to select appropriate time windows. Currently, TELVEL comprises about 30 subroutines and requires 65 K core storage. Approximately 20 K of the storage requirement is due to use of the proprietary graphics package DISSPLA^R. S^3 is now developing its own site-independent graphics package to enhance program transportability and simultaneously reduce storage requirements (to about 10 K for graphics).

SWIP is currently a batch-run program with input parameters specified in namelist statements and free-format reads. It is not configured to directly read the TELVEL output file, but instead requires text editing by the operator. SWIP writes results to a disk file.

SURWAV is also currently a batch-run program with namelist inputs. It writes its synthetic seismograms in SDL format.

The three programs mentioned above were developed independently of each other; the interfacing and data transfer between the programs is currently being streamlined. File structure is being reformatted to be consistent between the programs and to minimize operator effort.

The two batch codes SWIP and SURWAV are also being redesigned to be interactive and to automate as many steps as possible. While this requires a significant amount of code development, it should greatly reduce the amount of time necessary to obtain path corrections after the modifications are completed.

IX. OBJECTIVES AND RECOMMENDATIONS

Our primary objective under this contract is to develop and transfer to VSC the software required to obtain path corrections. We are now in the process of modifying our existing codes to make them easy to use and to make the determination of path corrections as rapid as possible. As soon as this is accomplished, the codes will be transferred to VSC and adapted to be consistent with the VSC file structure and computer facilities. They will also be adapted to interface with other codes at VSC such as the moment tensor inversion package being supplied by Sierra Geophysics which will use the path corrections.

We are also attempting to improve the method of estimating the attenuation coefficients. In general, the Rayleigh wave spectra do not contain enough information to determine the attenuation coefficients frequency by frequency. It is necessary to restrict the allowable Q models in some way. There are several possible methods of doing this. If detailed attenuation studies have been done in, or near, the area of interest, a published Q model may be available. Another possibility is to make Q a function of shear velocity or shear modulus since low Q zones typically correlate with regions of lower shear velocity. After an initial trial Q model is selected, it may be modified by changing a restricted number of free parameters and comparing the synthetic with the observed seismograms to obtain an improved Q model and improved attenuation coefficients.

In addition to developing and transferring the codes, we are preparing user manuals to accompany them. While the codes are designed to obtain path corrections, they are useful for a wide variety of other tasks and should be a valuable addition to the VSC computing facility.

X. REFERENCES

- Anderson, D. L., A. Ben-Menahem, and C. B. Archambeau (1965), "Attenuation of Seismic Energy in the Upper Mantle," JGR, 70, pp. 1441-1448.
- Archambeau, C. G., E. A. Flinn, and D. G. Lambert (1966), "Detection, Analysis, and Interpretation of Teleseismic Signals, 1, Compressional Phases from the SALMON Event," JGR, 71, pp. 3483-3501.
- Bache, T. C., W. L. Rodi, and D. G. Harkrider (1978), "Crustal Structures Inferred from Rayleigh Wave Signatures of NTS Explosions," BSSA, 68, No. 5, pp. 1399-1413.
- Cheng, C. and B. J. Mitchell (1981), "Crustal Q Structure in the United States from Multi-Mode Surface Waves," BSSA, 71, No. 1, pp. 161-181.
- Dobrin, M. B. (1976), Introduction to Geophysical Prospecting, McGraw Hill, New York.
- Dziewonski, A. M., J. Bloch, and M. Landisman (1969), "A Technique for the Analysis of Transient Seismic Signals," BSSA, 59, pp. 427-444.
- Dziewonski, A. M., J. Mills, and S. Bloch (1972), "Residual Dispersion Measurement - A New Method of Surface Wave Analysis," BSSA, 62, No.1 pp. 129-139.
- Harkrider, D. G. (1964), "Surface Waves in Multilayered Media I. Rayleigh and Love Waves from Buried Sources in a Multilayered Elastic Half Space," BSSA, 54, pp. 627-629.
- Harkrider, D. G. (1970), "Surface Waves in Multilayered Media II. Higher Mode Spectra and Spectral Ratios from Point Sources in Plane-Layered Earth Models," BSSA, 60, pp. 1937-1987.
- Herrin, E., and T. Goforth (1977), "Phase-Matched Filtering: Application to the Study of Rayleigh Waves," BSSA, 67, pp. 1259-1275.
- Jackson, D. D. (1972), "Interpretation of Inaccurate, Insufficient and Inconsistent Data," Geophys. J. Roy. Astron. Soc., 28, pp. 97-109.
- Jordan, T. H. (1972), "Estimation of the Radial Variation of Seismic Velocities and Density in the Earth," Ph.D. Thesis, California Institute of Technology, Pasadena, California.

Landisman, M., A. M. Dziewonski, and Y. Sato (1969), "Recent Improvements in the Analysis of Surface Wave Observations," Geophys. J., 17, pp. 369-403.

Landisman, M., A. M. Dziewonski, Y. Sato, and R. Masse (1968), "Preliminary Report on Recent Improvements in the Analysis of Surface Waves," Nuovo Cimento, Suppl 6, pp. 126-131.

Rodi, W. L., J. M. Savino, T. G. Barker, S. M. Day, and T. C. Bache (1978), "Analysis of Explosion-Generated Surface Waves in Africa, Results from the Discrimination Experiment and Summary of Current Research," Systems, Science and Software Report SSS-R-78-3653, submitted to Advanced Research Project Agency, April.

Wiggins, R. A. (1972), "The General Linear Inverse Problem: Implications of Surface Waves and Free Oscillations for Earth Structure," Reviews of Geophysics, 10, pp. 251-285.